All you need is shape: predicting shear banding in sand with LS-DEM

Reid Kawamoto, Edward Andò, Gioacchino Viggiani,
José E. Andrade

PII: S0022-5096(17)30658-0
DOI: 10.1016/j.jmps.2017.10.003
Reference: MPS 3197

To appear in: *Journal of the Mechanics and Physics of Solids*

Received date: 25 July 2017
Revised date: 5 October 2017
Accepted date: 6 October 2017

Please cite this article as: Reid Kawamoto, Edward Andò, Gioacchino Viggiani, José E. Andrade, All you need is shape: predicting shear banding in sand with LS-DEM, *Journal of the Mechanics and Physics of Solids* (2017), doi: 10.1016/j.jmps.2017.10.003

All you need is shape: predicting shear banding in sand with LS-DEM

Reid Kawamoto[a], Edward Andò[b], Gioacchino Viggiani[b], José E. Andrade[a*]
[a] *Division of Engineering & Applied Science, California Institute of Technology, Pasadena, CA 91125, USA*
[b] *Grenoble-INP / UJF-Grenoble 1 / CNRS UMR 5521, Laboratoire 3SR, Grenoble, France*

Abstract

This paper presents discrete element method (DEM) simulations with experimental comparisons at multiple length scales—underscoring the crucial role of particle shape. The simulations build on technological advances in the DEM furnished by level sets (LS-DEM), which enable the mathematical representation of the surface of arbitrarily-shaped particles such as sands. We show that this ability to model shape enables unprecedented capture of the mechanics of granular materials across scales ranging from macroscopic behavior to local behavior to particle behavior. Specifically, the model is able to predict the onset and evolution of shear banding in sands, replicating the most advanced high-fidelity experiments in triaxial compression equipped with sequential X-ray tomography imaging. We present comparisons of the model and experiment at an unprecedented level of quantitative agreement—building a one-to-one model where every particle in the more than 53,000-particle array has its own avatar or numerical twin. Furthermore, the boundary conditions of the experiment are faithfully captured by modeling the membrane effect, as well as the platen displacement and tilting. The results show a computational tool that can give insight into the physics and mechanics of granular materials undergoing shear deformation and failure, with computational times comparable to those of the experiment. One quantitative measure that is extracted from the LS-DEM simulations that is currently not available experimentally is the evolution of three dimensional force chains inside and outside of the shear band. We show that the rotations on the force chains are correlated to the rotations in stress principal directions.

1 Introduction

Despite its familiarity as an everyday material, the mechanical behavior of sand is complex. Sand can be modeled either as a continuous medium responding to Cauchy stress or as an assembly of individual particles following Newton's laws. Continuum models of sand [36, 50] are in demand to analyze field problems, and by their very nature they ignore particles and make use of such abstract concepts as stress and strain. In general, these models work acceptably; however, they fare less well in the commonplace yet complex scenario where strain is localized in regions so small that the granular structure cannot safely be ignored (*e.g.,* landslides, hourglass orifice flow). Models such as micropolar theory [28] inherently possess a length scale that allow them to capture strain localization such as shear banding [38]; however, studies have been limited to 2D conditions [14, 53] and many of their parameters' physical interpretations are not known and must be back-calculated from experimental data [15]. Thus, in order to handle 3D strain localization problems, it is generally agreed that an explicit modeling of the particle scale is needed.

As an alternative to continuum modeling, the discrete element method (DEM), directly simulates the interactions between thousands of spherical particles with physical, well-understood parameters such as particle size, stiffness, and coefficient of friction [13]; however, DEM does not adequately reproduce the

*Corresponding author. E-mail: jandrade@caltech.edu (José E. Andrade)

bulk behavior due to its poor representation of reality as sand particles (and many other types of particles!) are far from spherical. DEM's lack of ability to capture particle shape has spurred the development of variants able to capture particle shape, ranging from sphere clumping [20] to polyhedra [22] to ellipsoids [46, 59] to NURBS [35]. While clumping- and polyhedra-based methods can approximate the volume and general shape of sand particles, it has been shown experimentally and computationally that not only do the overall shape of particles ("sphericity") affect bulk granular behavior, but surface curvature at a lower, local scale ("roundness") also affects behavior [10, 26]. Unfortunately, clumping methods usually underestimate and polyhedra methods overestimate roundness unless a very large number of spheres or vertices are used [19]; however, "a 3D DEM simulation using a statistically valid number of clumps to faithfully simulate a real soil problem is still somewhat unrealistic" [60]. Ellipsoid-based particles usually overestimate roundness and are inherently convex. Although clumping, polyhedra, and ellipsoid methods have had modest success in replicating experimental results at the bulk scale [33, 31, 54], they have not been compared to experimental results at lower length scales, such as that of strain localization. NURBS-based methods accurately capture particle shape at both length scales and can accurately simululate granular behavior in shear bands, but are computationally time-expensive and have only been able to simulate unit cells of about one thousand particles at most [34]. One method of overcoming these *impasses* in both continuum and discrete modeling is the avatar paradigm, able to both characterize and simulate the behavior of granular assemblies through a DEM framework that characterizes particle shapes ("avatars") directly from experimental images, can simulate laboratory-scale amounts of particles (over 50,000), and captures the same 3D strain localization trends seen in experiments.

The avatar paradigm is also significant in that it helps to close the gap between experiments and simulations of granular materials; of the research that exists in investigating granular materials at the particle scale, there are broadly two camps: those who seek to characterize granular assemblies, often through experiments involving X-ray computed tomographic (XRCT) scans or photoelastic discs, and those who seek to simulate granular behavior, typically through DEM, with unfortunately little integration and validation between the two camps. In recent years, an overarching characterization and simulation framework, the avatar paradigm, has been developed. It consists of two parts: one, level set imaging (LS-Imaging) [56], which characterizes granular assemblies from XRCT images into avatars, or mathematical representations of individual particles within the assemblies, and two, the level set discrete element method (LS-DEM) [30], a DEM variant which can take avatars from LS-Imaging as an input and simulates their mechanical behavior.

LS-Imaging is the cutting edge in high-fidelity particle-scale characterization. Characterization of granular materials has come a long way since the days of "destructive" methods, which involved dismantling experimental specimens to measure particle-scale quantities [40], and 3D XRCT scans and other methods of digital imaging of experiments are now the norm in experimental particle-scale mechanics [42, 2]. Increases in image fidelity and resolution have led to the current state of the art characterization approach of LS-Imaging, which invokes the use of LS methods to extract surfaces of individual particles ("avatars") from XRCT images [18, 32, 56].

Although characterization techniques such as the aforementioned LS-Imaging have seen tremendous progress, they lack the ability to probe one crucial aspect of granular materials: interparticle contact forces. The stress-force-fabric relationship derived from interparticle contact forces [45] has been shown to be one of the key ingredients in the description of constitutive models for granular materials. Therefore, a micromechanical model such as DEM [13] remains a necessary component for the inference of contact forces and related quantities. LS-DEM is one such model which is able to handle real, complex particle morphologies which enabled reproduction and prediction of the bulk behavior of small experimental specimens consisting of about 3,000 particles each [30].

In this study, the avatar paradigm is built upon and used to characterize and simulate the behavior of a complete and much larger experimental specimen of natural sand, this time consisting of over 53,000 particles, reproducing the behavior of the experiment across three scales: macroscopic, local, and particle level. At the macroscopic level, the simulations using LS-DEM capture very closely the macroscopic stress-strain curve and the dilatancy-strain curve. These results have been obtained before using continuum models and well-calibrated DEM models such as [52, 31]. However, in this study, the results are able to go to deeper levels of prediction, which have not been attained before. For example, at the local level, the simulations show striking similarity with shear strain levels in the shear band and other

parts of the specimen. Furthermore, the model is able to predict the shear band orientation, inclination and thickness. This is something where both continuum and discrete models have struggled in the past. Finally, at the particle level, the model predicts particle rotations that on average compare well with those obtained in the experiment. Well beyond reproduction, the avatar paradigm affords the ability to see the evolution of interparticle forces, which are currently impossible to obtain from regular experiments, and which are an active area of research for single-crystal spherical particles [24]. Two modeling advancements afford the avatar paradigm higher fidelity: shape and more accurate boundary conditions. We present a model to replicate the boundary conditions of triaxial experiments. In particular, the deformability of the rubber membrane confining the specimen is modeled, as well as the displacement and rotation of the loading platen. Results show that these features are necessary to capture the evolution observed in the experiment, especially the onset and evolution of shear banding. By analyzing the kinematics and interparticle forces in the shear band, insights are gained regarding its formation, positioning, and evolution.

2 The Experiment: Triaxial Compression Test and Imaging of Specimen

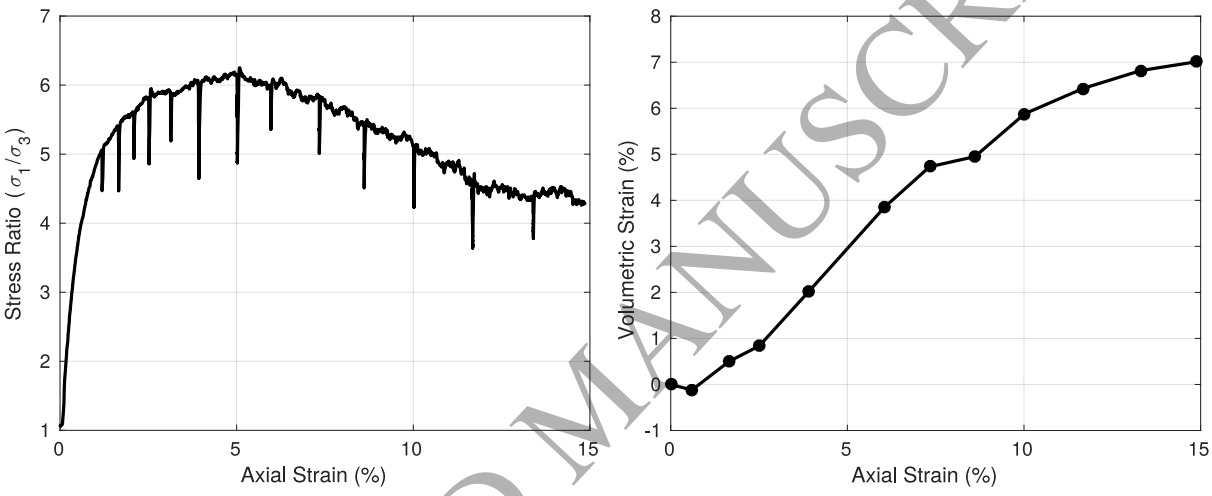

Figure 1: Stress-strain responses from the experiment. Positive values of volumetric strain indicate dilation. The stress relaxation in the stress-strain response is because axial loading is stopped during the imaging process. It is observed that, during imaging, no granular rearrangement takes place, which implies that stopping axial loading for imaging has a negligible impact on experimental results.

The experiment considered herein is a triaxial compression test on a small specimen of HN31 Hostun sand, which is performed within an X-ray scanner. The results of this test have appeared previously in [4] and are summarized here; more details can be found in [3]. The triaxial apparatus is much smaller than those used in conventional soil mechanics testing, and the specimen itself measures only 11 mm in diameter and 22 mm in height. This is because of constraints of the field of view of the XRCT imaging equipment, which is chosen to be able to adequately capture the features of individual particles, which in turn limits the specimen size. Nevertheless, the size of the sample is large enough to be representative of a continuum response of the material, displaying classic features such as stress-strain and volumetric responses observed in triaxial tests on standard-sized specimens, as well as the appearance of shear banding.

Hostun HN31 has $D_{50} = 338$ μm, and poor grading. Particles are angular and non-spherical, especially compared to other 'standard' sands used in geomechanics research, such as Toyoura and Ottawa sand. Hostun sand is chosen for its particularly challenging particle shapes to showcase the ability of LS-DEM to simulate particles of arbitrary shape.

The experiment is as follows: a flexible latex membrane 10 mm in diameter and 0.3 mm thick is stretched into a cylindrical mould and filled with Hostun sand using dry pluviation. On the top and bottom of the specimen, the sand is in contact with two ceramic discs, one of which, together with a metal cylinder onto which the loading ram pushes, makes up the loading platen (this important detail is further discussed in

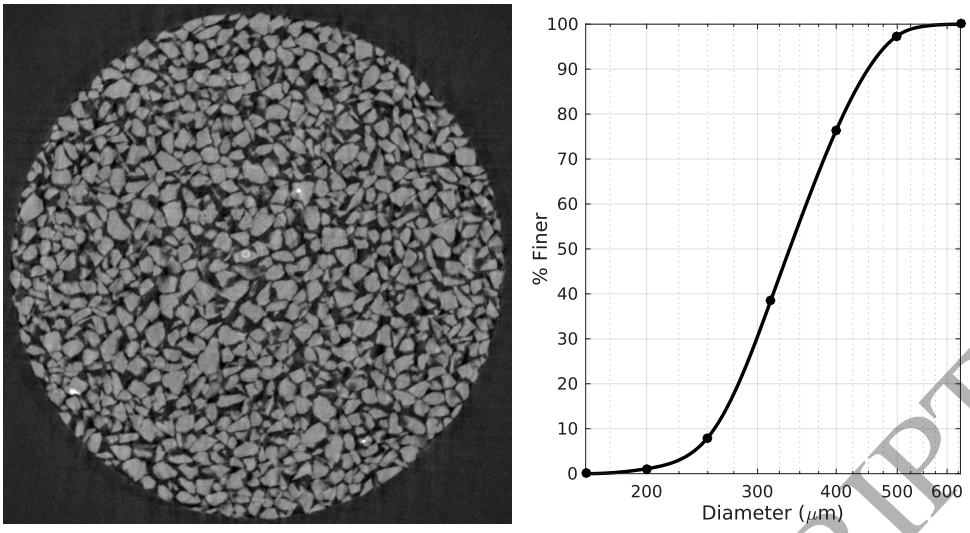

Figure 2: 3-D XRCT image slice of the experimental specimen prior to triaxial compression and the specimen's particle size distribution.

Section 4.2). The specimen is then compressed isotropically by increasing the radial cell pressure with the ram out of contact to 100 kPa, and then compressed triaxially by keeping the cell pressure constant at 100 kPa and prescribing a displacement to the ram. Air can escape or enter the through a small hole in the ceramic disk opposite the loading platen which gives for drained loading conditions. The ram is loaded at a rate of 12 μm per minute, except when loading is suspended to image the specimen, to a total axial strain of 15% (3.3 mm).

The "classic" triaxial test results of the experiment are shown in Figure 1 and are typical of a drained experiment on sand. The stress ratio σ_1/σ_3, the ratio of axial stress to cell pressure, increases to a peak around 5% axial strain, then decreases and appears to level off around 13% axial strain. Meanwhile, the specimen undergoes a slight contraction at the beginning of loading and then dilates until the end of loading when it seems to level off. Other specimens of Hostun sand tested in the same apparatus experienced similar behavior, so this particular experiment is representative of Hostun sand tested in the particular apparatus under the particular loading conditions and offers a good reproduction of key features of the mechanical response of larger specimens [3].

In addition to the triaxial test itself, the specimen is also imaged at various load stations throughout loading. At each imaging station, the specimen is rotated through 360° while taking 1024 X-ray projections, in about two hours. The X-ray projections are then used to reconstruct a three-dimensional image by filtered backprojection [23]. The resulting three-dimensional image has a pixel size of 14.7 μm/pixel edge, which means that the 11mm × 22mm specimen has a total of about 750 × 750 × 1500 voxels. A slice of the three-dimensional reconstructed XRCT image and the specimen's particle size distribution curve are shown in Figure 2.

3 Bridging the Experiment and Computation: The Avatar Specimen with LS-Imaging

In order to be able to simulate the experiment, it is necessary to convert the experimental output into a format palatable by computational methods. This intermediate step consists of converting the 3D XRCT image taken from the load station after isotropic compression but before triaxial compression into an avatar specimen, *i.e.,* a computational representation of the specimen that can be simulated with LS-DEM. The XRCT image in this study has a resolution of 15 μm/voxel (D_{50} = 23 voxels), and dimensions of approximately 750×750×1500 voxels. First, the image is binarized via thresholding [41], which determines which voxels are solids and which voxels are voids. Then, the binarizared image is segmented using watershed algorithms [7], which label the solid voxels as belonging to individual particles. The segmentation, as well as the gradient of the grayscale image, filtered using a non-local means filter, are used as inputs to level set-imaging algorithms [18, 32, 56], which yield the particle

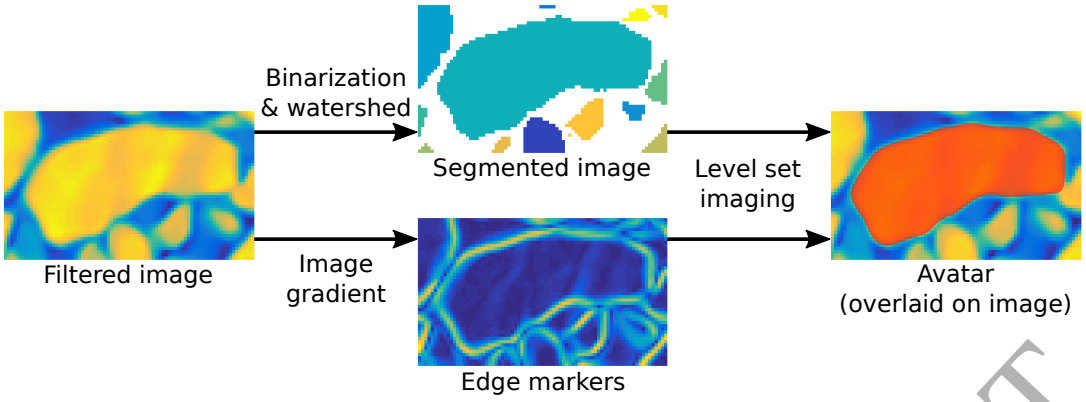

Figure 3: Avatar conversion process for a single avatar. The filtered image is both segmented and used to find particle edges, which are then fed into the level set imaging algorithm, which outputs an avatar. Note that these operations are performed in three dimensions; a slice is shown here for clarity.

"avatars" that are used in this study. The accuracy of the avatars in terms of their ability to preserve the same fabric as the particles in the image has been investigated in [57]. Figure 3 illustrates the avatar conversion process described above.

4 Computations: Modeling and Simulation of Avatar Specimen

The simulation of the avatar specimen is performed using LS-DEM [30] under the same external loading conditions as the experiment. Since one of the objectives of this study is to provide the best possible replication of the experiment, two crucial experimental details are implemented *in silico*: the actual kinematics of the loading platen that compresses the specimen and the flexible membrane used to confine the specimen.

4.1 LS-DEM

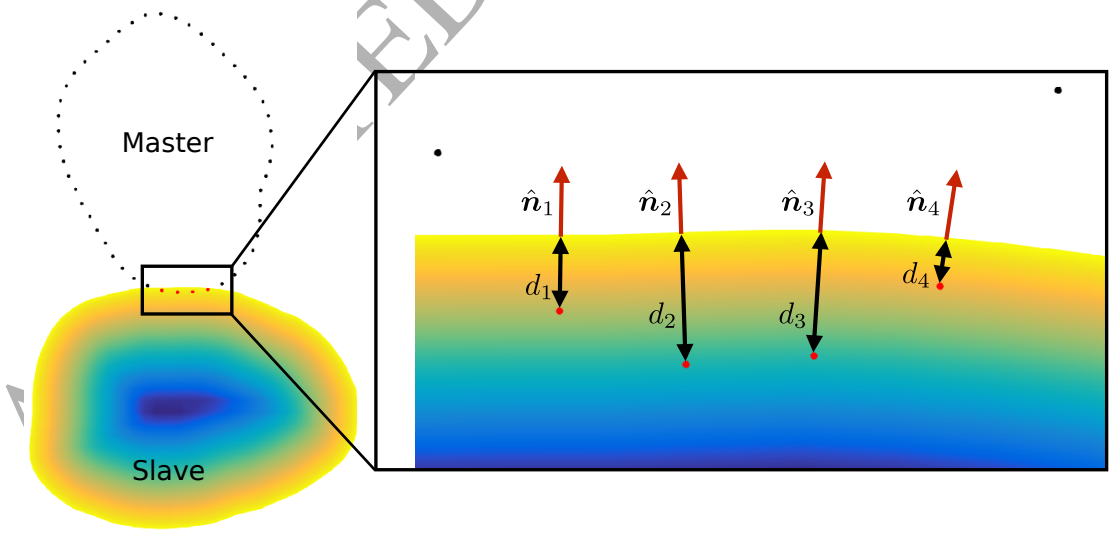

Figure 4: Contact between two particles in LS-DEM. Particles shown here are 2D for simplicity; however, 3D particles are used in this study. Penetration depths are exaggerated for clarity.

LS-DEM is a variant of DEM that models particle shape via level set functions that represent the geometry of constituent particles [30]. When used to represent a particle in LS-DEM, a level set function is an implicit function whose value, at a given point, is the signed distance from that point to the surface of the particle: negative if the point lies inside the particle, positive if the point lies outside, and zero

if the point lies on the particle's surface. In a DEM framework, this formulation is convenient because two of the most important ingredients in DEM contact detection, interparticle penetration distance and contact normal, are given as

$$d = \phi(\boldsymbol{x})$$
$$\hat{\boldsymbol{n}} = \boldsymbol{\nabla}\phi(\boldsymbol{x})$$

for a level set function ϕ and given point $\boldsymbol{x}$, where d and $\hat{\boldsymbol{n}}$ are the penetration distance and contact normal, respectively. In practice, the values of a level set function are stored at discrete points on a grid, and interpolation is used to compute values between grid points.

To determine contact between two particles, a master-slave approach is used, where the surface of the master particle is discretized into nodes. Each node of the master particle is checked against the level set function of the slave particle, and if the value of the level set function is negative for any node, contact exists and forces and moments are computed for each penetrating node, which are then summed to give the total interparticle forces and moments. Figure 4 illustrates interparticle contact in LS-DEM.

To compute the the normal force, any contact model such as linear contact or Hertzian contact [27] may be used; in this study, a linear contact model is used (if a Hertzian model is used, the level set formulation allows local radii of curvature to be computed easily). The tangential force is computed via a Coulomb friction model.

The LS-DEM formulation only affects contact detection and the computation of interparticle forces and moments; other aspects such as time integration are not specific to LS-DEM and thus any implementation can be used such as those used in DEM or contact dynamics [25]. In this study, an explicit time integration scheme identical to that in DEM is used [35, 58].

4.2 Platen Modeling

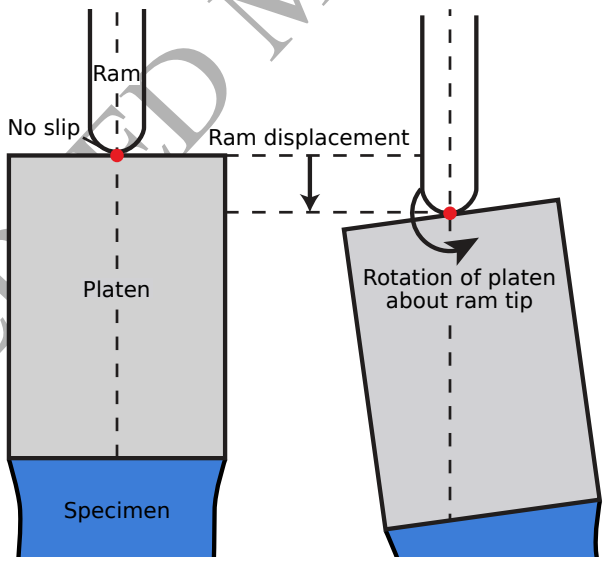

Figure 5: Behavior of the platen. The platen does not slip on the loading ram, so it is limited to movement in the vertical direction and rotation about the ram tip.

As shown in Figure 5, the loading platen is compressed axially by a ram, which is observed not to slip on the platen due to friction. The no-slip condition limits the platen's degrees of freedom to (1) vertical displacement, prescribed by the movement of the ram, and (2) rotation about the ram-platen contact point. In the simulation, the platen is modeled using a cylindrical discrete element with the same properties as the platen in the experiment, shown in Table 1, and is only allowed to move vertically and rotate about the ram-platen contact point exactly as in the experiment. While the rotational behavior of the loading platen may be seen as an axis-angle rotation, it is more instructive to instead view the

Platen Parameter	Value	Units
Radius	7.5	mm
Height	11.4	mm
Density	2,500	kg/m^3
Normal stiffness	3.0×10^4	N/m
Shear stiffness	2.7×10^4	N/m
Friction coefficient	0.5	

Table 1: Values of parameters used in simulation of platen.

platen's kinematics as the lateral movement of the platen face that is in contact with the specimen, since the direction of this movement is related to the direction of shear in the specimen.

4.3 Membrane Modeling

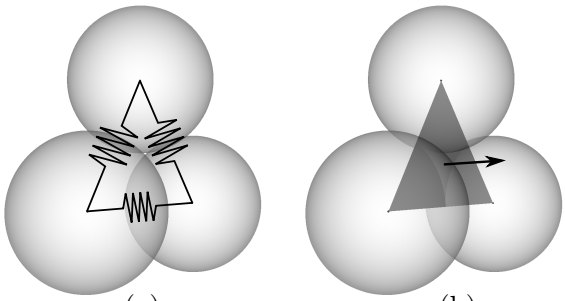

Figure 6: Triangulation of three membrane spheres. (a) Neighboring spheres are connected by normal and shear springs. (b) Pressure is applied in the direction of the inward normal to each face.

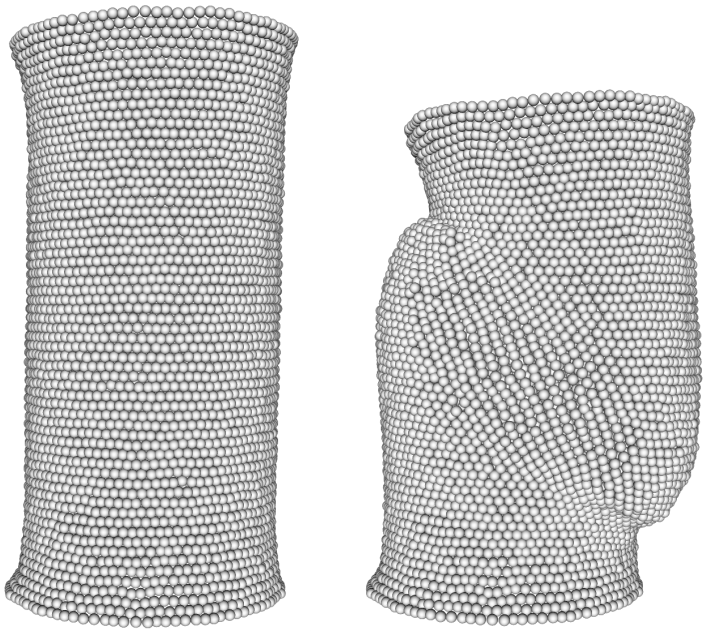

Figure 7: Membrane (a) under isotropic stress and (b) at the end of triaxial loading.

As mentioned previously, the membrane is made out of latex and closely follows the deformation of the specimen. Membranes and other soft materials such as textiles have been modeled using DEM [6, 12],

Membrane Parameter	Value	Units
Sphere radius	0.22	mm
Number of spheres	5,760	
Diameter	10	mm
Normal bond stiffness	100	N/m
Shear bond stiffness	100	N/m
Normal stiffness	3.0×10^4	N/m
Shear stiffness	0	N/m

Table 2: Values of parameters used in simulation of membrane.

and in this study, the membrane is modeled in a DEM-like fashion by using thousands of bonded spheres in a hexagonal pattern shaped into a hollow cylinder, as shown in in Figure 6. The spheres' centers are triangulated, and adjacent spheres are connected by both normal and shear springs. In addition to stiffness when interacting with adjacent spheres, the spheres also have a stiffness when interacting with particles in the assembly. Confining pressure is applied in the direction of the inward normal to each face, where faces are defined by the triangles whose vertices are the centers of three adjacent spheres, and multiplied by the area of each face; the resulting force is distributed evenly to each component sphere. The size and stiffness of the membrane spheres are calibrated to values that allow them to stay aligned and not form gaps that would let particles escape, see Table 2. Finally, the top and bottom rows of membrane spheres are fixed to their respective platens to represent the friction between the membrane and platen. The ability of the membrane to deform is shown in Figure 7.

4.4 Putting it all together: the LS-DEM Simulation

Particle Parameter	Value	Units
Number of particles	53,939	
Density	2,500	kg/m^3
Normal stiffness	3.0×10^4	N/m
Shear stiffness	2.7×10^4	N/m
Friction coefficient	0.55	

Table 3: Values of parameters used in simulation of particles.

As mentioned previously, the simulation of triaxial compression on the avatar sample is carried out using LS-DEM. To initialize the simulation, the particles are placed in the same positions as given by the avatar conversion process, the platens are put in the same positions as the experiment, and the membrane is fit around the specimen, which is then loaded isotropically to a pressure of 100 kPa, the same as that of the experiment. The specimen is then compressed triaxially by imposing a vertical displacement to the ram up to an axial compression of 15% while keeping confining pressure constant at 100 kPa. Please note that the loading rate of the simulation is higher than the loading rate of the experiment since using the same strain rate as the experiment would not be computationally tractable. However, parameters such as damping are calibrated to keep the simulation quasi-static. The simulation of 53,939 particles and 5,760 membrane particles was performed on San Diego Supercomputer Center's XSEDE cluster Comet using 480 cores and took 17 hours to complete, which is faster than the "wall time" for the experiment due to X-ray scanning time.

Figure 8 shows the avatar specimen at the beginning and end of triaxial loading. By the shape of the specimen at the end of the test, a shear band appears to have formed from the top-left to the bottom-right. The axes in the visualization have been aligned to show this deformation.

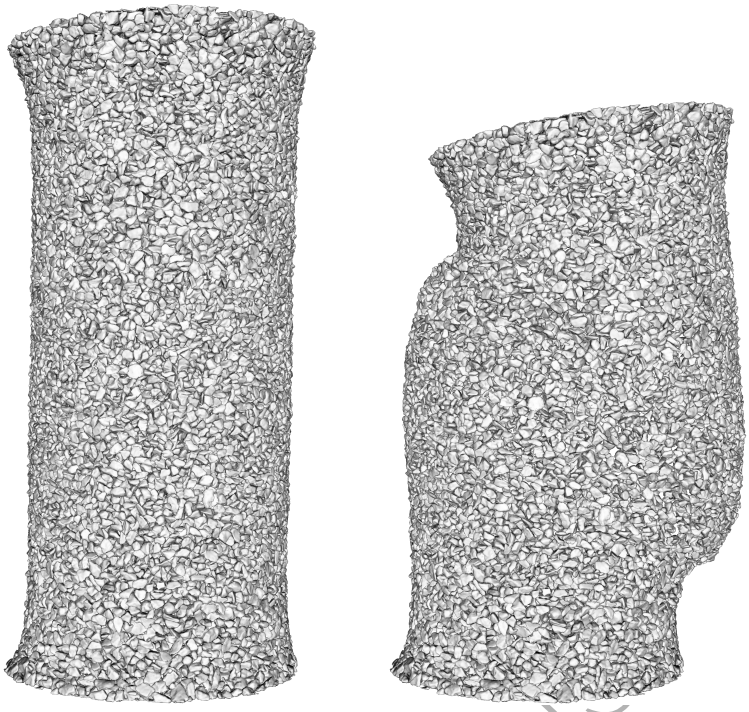

(a) (b)

Figure 8: Avatar specimen (a) under isotropic stress and (b) at the end of triaxial loading.

5 Validation of Simulation

Due to the wealth of information provided by the triaxial test and XRCT imaging, the simulation is validated by comparing its results to the experimental results at three length scales: the macroscopic scale, which considers values measured from the boundary conditions such as global volume changes and axial stress, the local scale, which considers the behavior of particles with respect to their neighbors, and the particle scale, which considers the kinematics of individual particles.

While the LS-DEM model parameters are calibrated to match the macroscopic experimental results in Figure 1, it is important to note that all of the parameters used have roots in physics. For example, the value of interparticle friction of 0.55 that is used in the simulation is within the range of experimentally observed values of interparticle friction [49] in sands.

5.1 Macroscopic Behavior

As Figure 9 shows, there is good agreement in both macroscopic stress ratio σ_1/σ_3 and volume change as a function of axial strain between the experiment and LS-DEM simulation. As axial loading progresses, the stress ratio increases to a maximum value then softens, tending towards a residual value after 10% axial strain. The specimen exhibits a slight initial decrease in volume then dilates before reaching a maximum volume around 10% axial strain and stays roughly at that volume for the remainder of axial loading. The peak stress and the largest incremental change in volume both occur very close to the same axial strain (4%). This is in good agreement with classic stress-dilatancy theory and observations [47, 8, 39].

5.2 Local Behavior

In this study, the local results are found by looking at particle quantities with respect to their neighboring particles; specifically, the strain in the vicinity of each particle, which is computed using Cundall's best-fit strain [5], which represents the average deformation of a set of points undergoing displacement:

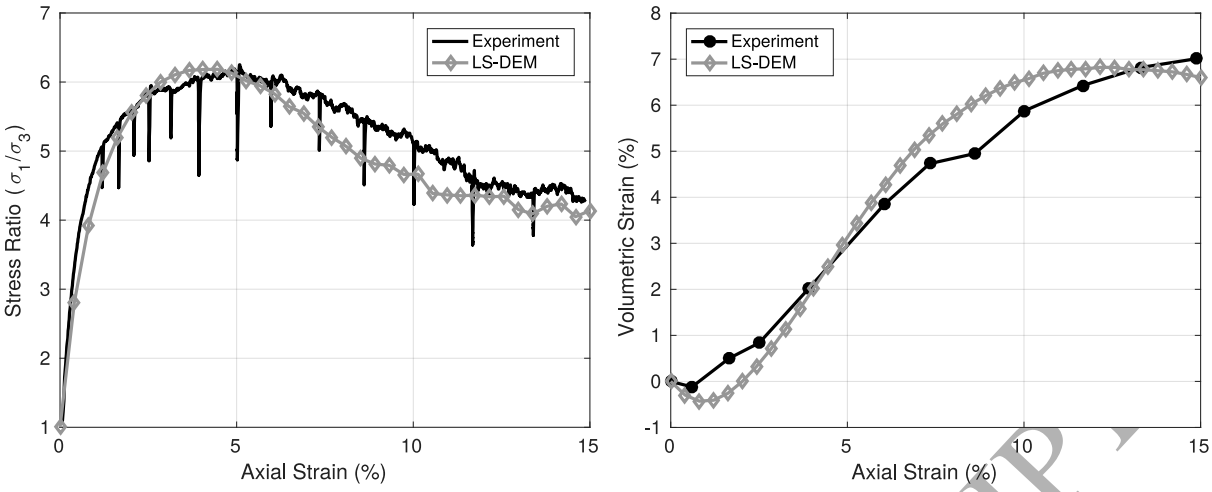

Figure 9: Macroscopic stress-strain responses from the experiment and LS-DEM simulation.

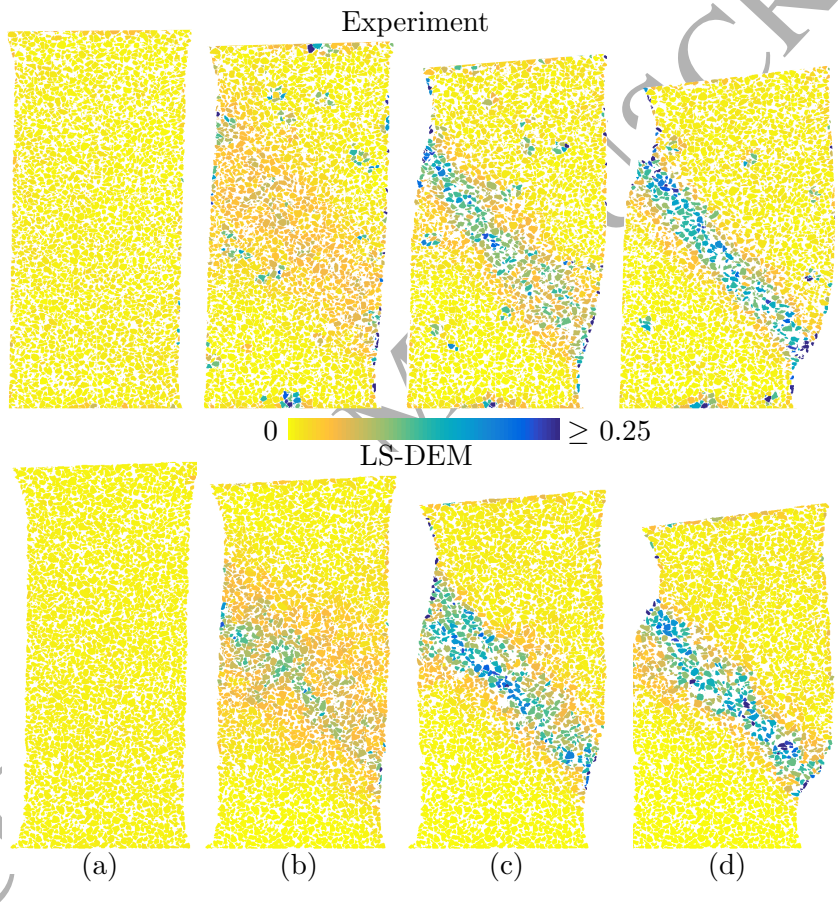

Figure 10: Experimental and simulation incremental local deviatoric strain between (a) 0.0 and 0.6%, (b) 3.9 and 5.1%, (c) 8.6 and 10.0%, and (d) 13.3 and 14.8% axial strain.

$$\left(\sum_{p=1}^{N_p} \tilde{x}_n^p \tilde{x}_m^p\right) \alpha_{ni} = \sum_{p=1}^{N_p} d\tilde{u}_i^p \tilde{x}_m^p \qquad n, m, i = 1, 2, 3 \tag{1}$$

where N_p is the number of points, $\tilde{\boldsymbol{x}}^p$ is the deviation of each point's position from the mean position, $d\tilde{\boldsymbol{u}}^p$ is the deviation of each point's displacement from the mean displacement, and Cundall's best-fit strain $\boldsymbol{\epsilon}$ is the symmetric part of $\boldsymbol{\alpha}$. In this study, the centroids of each particle in the specimen are triangulated and the local strain of a given particle is found by applying Cundall's best-fit strain to the particle centroid and its neighbor centroids as given by the triangulation. Finally, from Cundall's best-fit

strain, the deviatoric invariant ϵ_s is computed by [9]:

$$\epsilon_s = \sqrt{\frac{2}{3}} \|\boldsymbol{\epsilon} - \frac{1}{3}\mathrm{tr}(\boldsymbol{\epsilon})\boldsymbol{I}\| \tag{2}$$

Figure 10 shows the distribution of the incremental local deviatoric strain during four strain increments for a shear band-aligned slice through the center of both the experimental and computational specimens. Note that the slices have the same orientation in three-dimensional space. While there is generally good parity between the LS-DEM and experimental specimens, in the increment corresponding to the 3.9 to 5.1% axial strain increment (Figure 10b), the LS-DEM specimen shows higher deviatoric strain that is more localized than the experimental specimen. This is likely due to the fact that during that increment, the LS-DEM specimen reaches peak stress, but it is not until the end of that increment that the experimental specimen reaches peak stress.

5.3 Particle Behavior

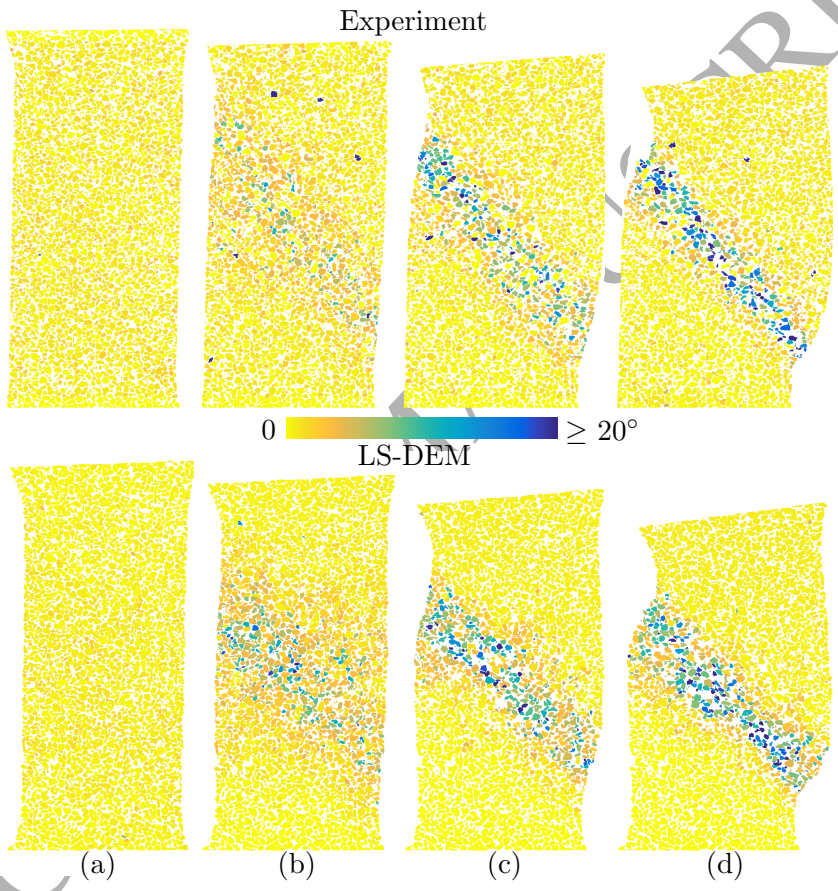

Figure 11: Experimental and LS-DEM incremental particle rotations between (a) 0.0 and 0.6%, (b) 3.9 and 5.1%, (c) 8.6 and 10.0%, and (d) 13.3 and 14.8% axial strain.

As a salient example of particle-scale quantities, particle rotations in the simulation are compared to those measured by particle tracking in the experiment. While they cannot be compared one-to-one, in other words, a particle and its avatar may not necessarily have directly comparable kinematics, they should strongly correlate in both an average sense and in regions where rotations are large, such as in the shear band. Figure 11 compares incremental particle rotations (*i.e.,* the angle of rotation in the axis-and-angle representation of 3D rotations) during four strain increments for a shear band-aligned slice through the center of both the experimental and computational specimens. The slices have the same orientation in three-dimensional space and the locations and quantities of incremental rotations are comparable. As with local deviatoric strain, and for the same reason, particle rotations are higher in the 3.9 to 5.1% axial strain increment.

6 Shear Band Investigation

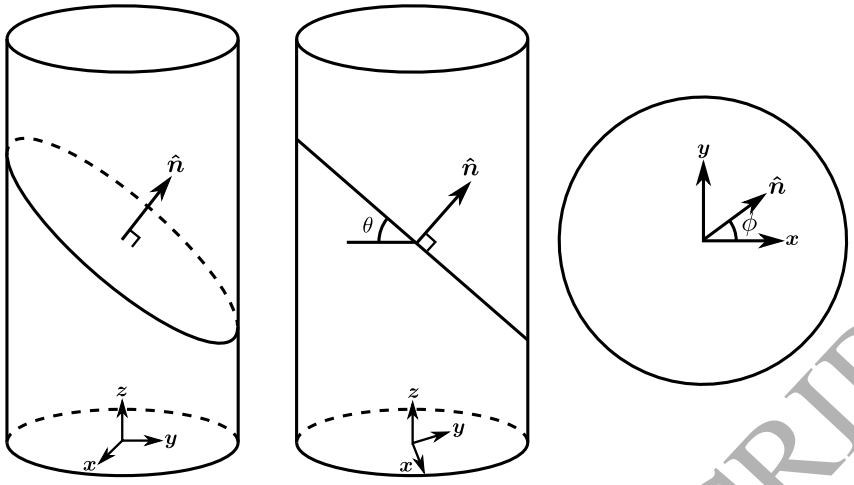

Figure 12: (a) Shear band and its normal $\hat{\boldsymbol{n}}$ in three-dimensional space, where z is the direction of loading, normal to the x-y plane. (b) The shear band inclination angle θ is measured with respect to the x-y plane. (c) The shear band orientation angle ϕ is measured in the x-y plane.

A shear band is a localized deformation pattern that is "smooth and continuously varying", characterized by very large amounts of shear strain, and formed when a ductile solid is deformed well past its elastic limit [48, 43]. In granular materials, the thickness of the shear band t_s is typically measured in multiples of the mean particle diameter D_{50} and varies with particle shape, specimen porosity, and mean stress [21]. In this study, t_s/D_{50} is found to be 10, which is consistent with values reported in literature [17] as well as the experiment itself [2] (for more, see 6.3).

The inclination of the shear band with respect to the plane orthogonal to the loading direction, represented by the inclination angle θ, has been found to be a function of the stress-strain state, with different theories dictating this inclination angle [51]. On the other hand, the orientation of the shear band *in* that plane, represented by the orientation angle ϕ, is correlated with the direction of the movement of the platen. Figure 12 illustrates the inclination and orientation angles of the shear band.

6.1 Shear Band Inclination

The Mohr-Coulomb yield criterion gives the shear band inclination angle, measured from the direction of minimum principal stress σ_3, which in a triaxial test is orthogonal to the loading direction, as

$$\theta_{MC} = 45^\circ + \frac{\phi_{\max}}{2} \tag{3}$$

where $\phi_{\max}$ is the maximum friction angle, which is achieved at peak stress.

Roscoe's solution for the shear band inclination angle [44] is

$$\theta_R = 45^\circ + \frac{\psi_{\max}}{2} \tag{4}$$

where $\psi_{\max}$ is the maximum dilatancy angle in the zone of deformation, also achieved at peak stress. The two solutions differ due to the non-associativity between stress and strain in granular materials; in the case of associativity, the solutions are equal.

With the discrete data available in the experiment and the simulation, the shear band can of course be measured geometrically. Since particle rotations and local deviatoric strains are very large in the shear band, best-fit planes are computed from the positions of particles whose rotations and local deviatoric strains are more than two standard deviations greater than the average incremental rotation and

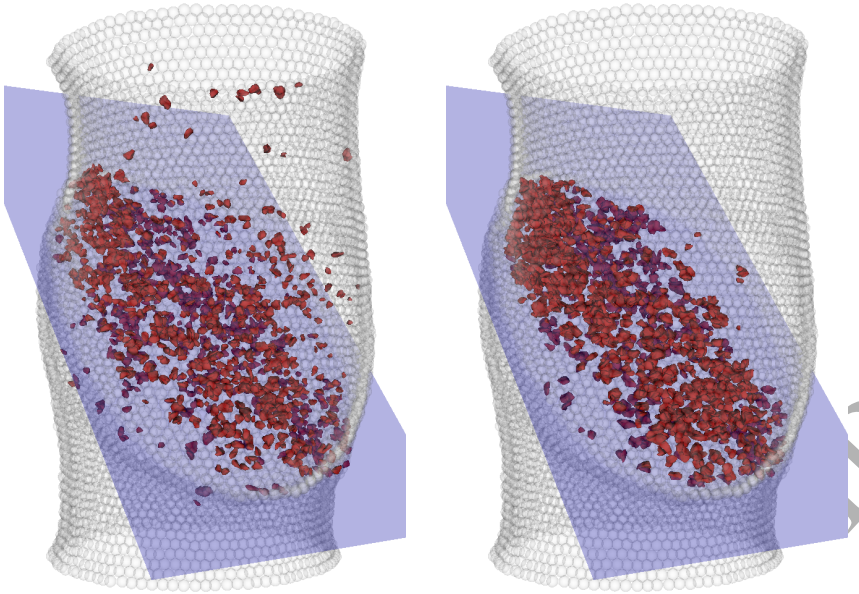

(a) (b)

Figure 13: Simulation results (increment between 14 and 15%). Particles in red are those with (a) incremental rotations or (b) incremental local deviatoric strains larger than two standard deviations more than the mean, and corresponding best-fit planes.

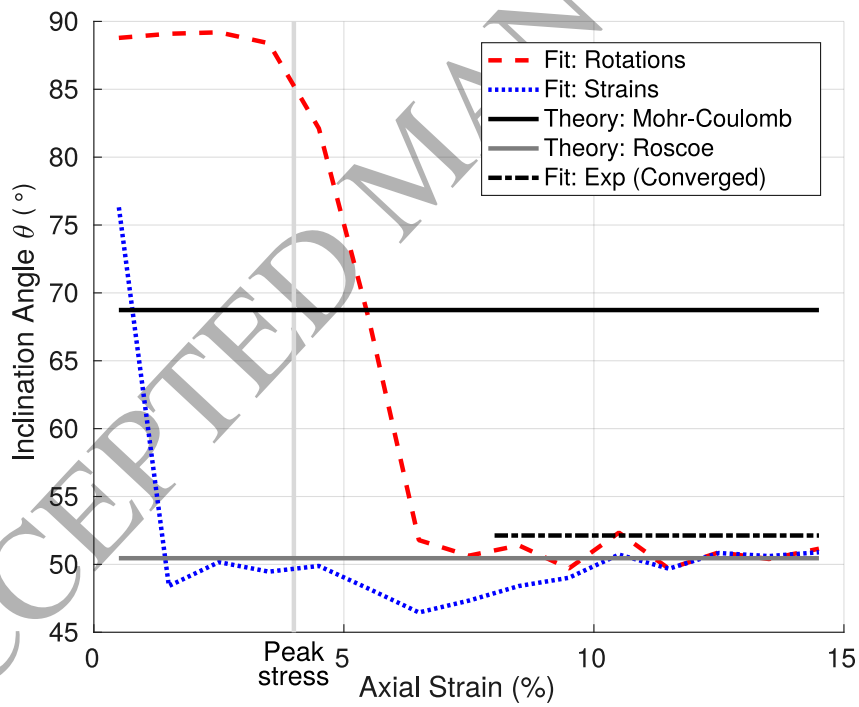

Figure 14: Shear band inclination computed from best-fit planes computed from particles with large incremental rotations and large incremental deviatoric strains, inclination predicted by Mohr-Coulomb and Roscoe theories, and the converged value of the inclination angle from experimental data.

deviatoric strain, respectively. Values are computed in increments of axial strain of 1%, between 0 and 15% total axial strain.

Figure 13 shows an illustration of shear band planes as defined by incremental rotations and local deviatoric strains from the 14-15% increment of axial strain in the simulation. Shear band planes are

computed for 15 values of strain, in increments of 1%, using the incremental local deviatoric strains and incremental rotations. Shear band volumes are defined as the planes (here, we choose the plane computed using incremental local deviatoric strains) plus a shear band thickness $t_s/d_{50} = 10$; thereafter the average stress and strain states in the shear band volumes are computed. The average stress $\bar{\boldsymbol{\sigma}}$ is given by Christofferson's equation [11]

$$\bar{\boldsymbol{\sigma}} = \frac{1}{V} \sum_{i}^{N_c} \boldsymbol{F}_i \otimes \boldsymbol{d}_i \tag{5}$$

where V is the volume, N_c is the number of contacts in the volume, and $\boldsymbol{F}$ and $\boldsymbol{d}$ are the interparticle force and branch vector, respectively, of each contact. From the average stress, the Mohr-Coulomb solution is found for the shear band inclination angle at the peak stress state. The average strain is computed using Cundall's best-fit strain in Equation 2 using all particle centroids in the shear band volume as the points, and Equation 4 is applied to find the Roscoe solution for the shear band inclination angle at the peak stress state.

Figure 14 summarizes the results computed from the best-fit planes corresponding to large local incremental rotations and deviatoric strains, the prediction from Mohr-Coulomb and Roscoe theories, and the converged value of the inclination angle from experimental data. There are two notable remarks about these results; first, the fit using strains seems to indicate the presence of, or at least a precursor to, a shear band far earlier than the fit using rotations. In fact, as early as 2% axial strain, long before peak stress at 4% axial strain, the deviatoric strain has already localized in a zone that aligns with the shear band. On the other hand, particle rotations do not align with the ultimate shear band angle until after peak stress is reached. Second, it appears as though Roscoe's solution for the shear band inclination angle is much closer (in fact, nearly identical) to the best-fit shear band inclinations compared to the Mohr-Coulomb solution.

6.2 Shear Band Orientation

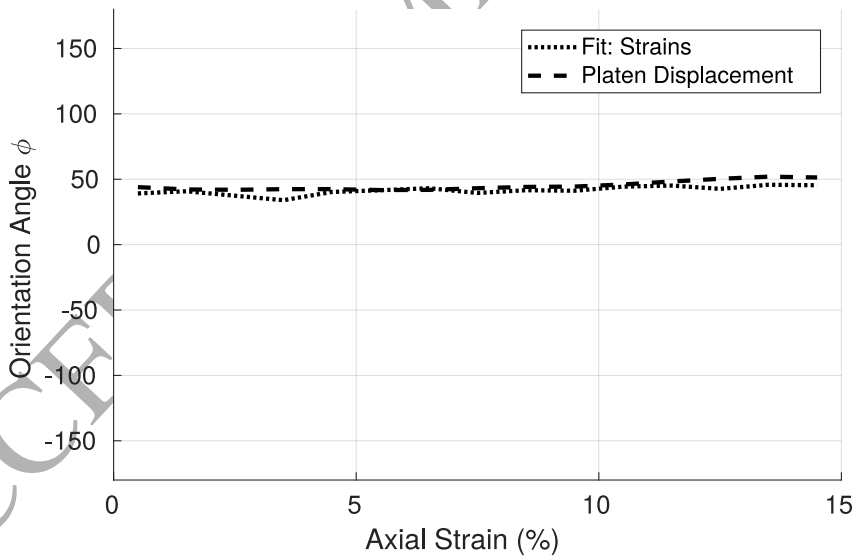

Figure 15: Shear band orientation angle computed from best-fit plane of large incremental local strains and incremental platen displacements.

Many experimental studies of shear bands have been performed in plane strain, such as plane strain compression, simple shear, or direct shear. This makes it easy to determine the orientation of the shear band, as it will not have any component in the direction of the third dimension. However, in a triaxial compression test, the shear band may orient itself in any direction within the plane orthogonal to loading.

Figure 15 shows that the shear band orientation angle ϕ is strongly correlated with the orientation of the incremental x-y displacements of the platen. While the displacement of the platen may seem random, a function of the specimen's natural tendency to shift laterally under vertical loading, much like

the buckling of a beam, it is important to note that the direction of shear throughout loading is constant, and if a coordinate system is defined such that two axes are aligned with the direction of loading and the lateral direction of platen displacement, the vast majority of shear in the specimen occurs along these two axes with little shear along the third axis, which makes some two-dimensional analysis possible.

6.3 Shear Band Thickness and Kinematics

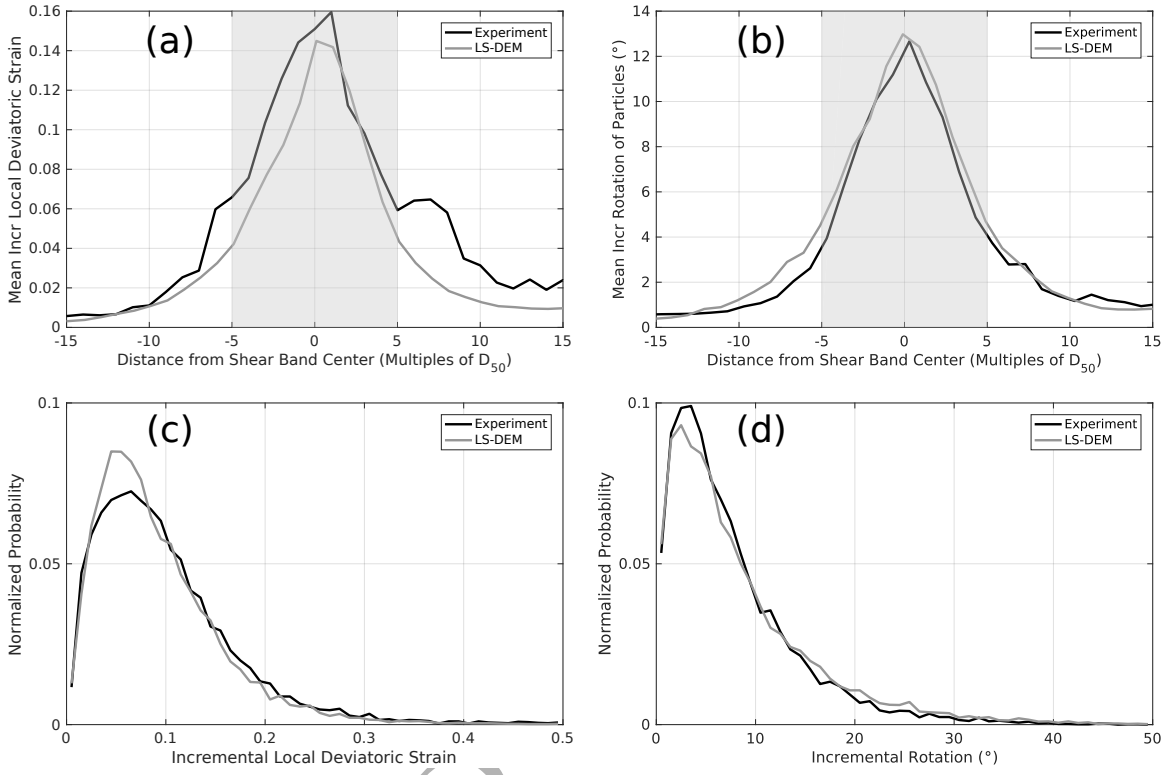

Figure 16: (a-b) Plots of mean incremental local deviatoric strain and mean incremental rotation between 13.3 and 14.8% axial strain versus distance from the center planes of shear bands in the experiment and simulation (which do not necessarily have the same location). The gray stripes represent a distance of $10D_{50}$, or 3.4mm, the thickness of the shear band. (c-d) Histograms of incremental local deviatoric strain and incremental rotation in the shear band (the gray stripes in a-b) during the same axial strain increment.

Another quantity of particular note is the thickness of the shear band. In Section 6.1, we use the fact that local deviatoric strains and particle rotations are much higher in the shear band to determine the location of the center plane of the shear band, but this gives no notion of the shear band's thickness. Figure 16a-b shows plots of the aforementioned quantities, local deviatoric strain and particle rotations, versus distance (in the normal direction of the shear band plane) from the center plane of the shear band, near the end of loading. These quantities are the highest near the center plane of the shear band and decay as a function of distance from the center of the shear band, as expected. The thickness of the shear band can be found through various methods [1] but for simplicity, we choose $t_s/d_{50} = 10$, represented by the gray stripe.

Figure 16c-d shows histograms of kinematics in the shear band (the quantities contained in the gray stripe in Figure 16a-b) in terms of incremental local deviatoric strains and incremental particle rotations, respectively, near the end of loading. In the experiment, the mean incremental particle rotation is 7.7° and the mean incremental local deviatoric strain is 0.100, while in the LS-DEM simulation those values are 8.4° and 0.092, respectively. The results indicate that, by the end of the experiment, the shear bands in both the experiment and simulation are quantitatively similar in terms of their kinematics.

6.4 Interparticle Forces and Stress

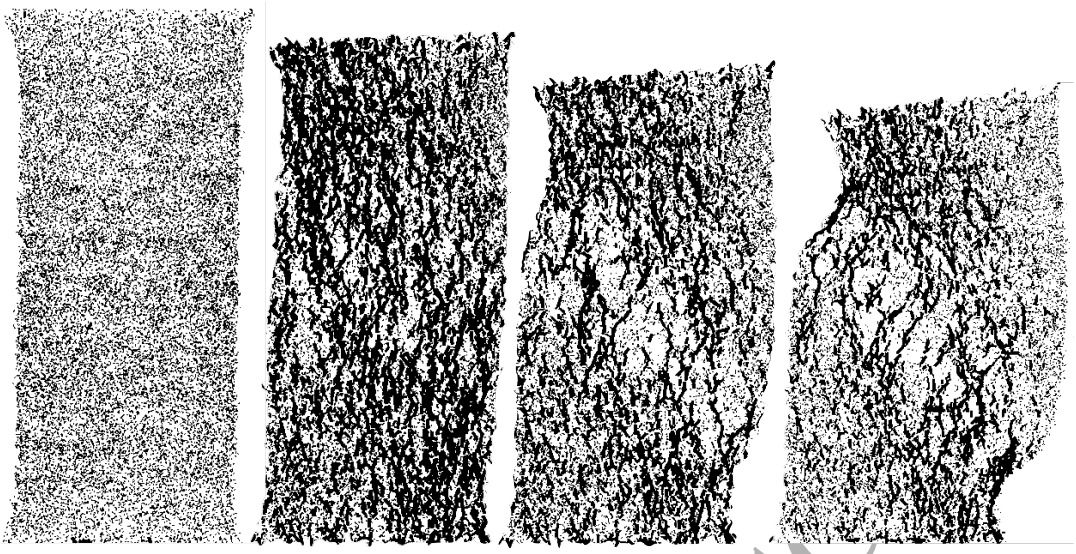

Figure 17: Interparticle forces in a shear band-aligned slice 1.4mm thick through the center of the specimen at (a) 0%, (b) 5%, (c) 10%, and (d) 15% axial strain. Thicker, longer lines represent larger interparticle forces.

Because interparticle forces are an inherent quantity in LS-DEM computations, LS-DEM provides the ability to enrich existing kinematic analyses (which can be observed in experiments) with analyses of forces and stresses (which cannot be obtained in this sort of experiment). Figure 17 shows the evolution of interparticle forces throughout loading in a shear band-aligned slice 1.4mm thick through the center of the specimen. Initially, interparticle forces are small and isotropic, having no directional bias, but at 5% axial strain, which is near the peak stress, interparticle forces become much larger and oriented in the direction of loading. However, as the shear band develops, the forces in the shear band and out of the shear band appear to lose coaxiality, which is most apparent in Figure 17d, where force chains seem to change direction as they pass through the shear band. The anisotropy and directionality of the interparticle forces can be quantified by a spherical histogram (referred to as a "rose diagram" in literature [29]) of forces, normalized by unit volume. Figure 18 shows the evolution of the distribution of forces inside and outside the shear band of the specimen between 0 and 15% axial strain. Between 0 and 5% axial strain, the forces become much more anisotropic and remain that way through 15% axial strain. In terms of directionality, inside the shear band, the forces seem to undergo a rotation between 5 and 15% axial strain, while outside the shear band, there is much less rotation. Given the effect that the distribution of interparticle forces has on stress via the "stress-force-fabric" relationship [45], one would expect the stress in the shear band to also rotate, and indeed, it is observed that the stress state in the shear band, computed via Eq. 5, undergoes rotation as loading progresses.

Figure 19 shows the inclination angle of the major principal stress σ_1 outside and inside the shear band. The grayed-out sections of the lines are computed using the shear band location at peak stress and show that before the shear band forms, the inclination angle is nearly vertical and similar inside and outside the location where the shear band forms. However, after the shear band forms, the inclination angle outside the shear band deviates by less than 2°. In stark contrast, inside the shear band the inclination of σ_1 essentially continuously decreases after the shear band forms, from almost 90° to 81°, with no sign of flattening by the end of loading. While the specimen undergoes very little volume change between 10-15% axial strain with very little change in the macroscopic stress ratio, which are necessary for critical state [37], the stress state in the shear band continues to rotate in this strain increment. Unfortunately, loading is terminated at 15% axial strain to match the experiment so a minimum value of the inclination angle of σ_1 is never observed, so it is thus questionable, in light of recent suggestions of a 'critical state fabric' [16], whether or not the specimen actually reaches critical state by the end of loading, and certainly provides an impetus for more research to be done on this subject.

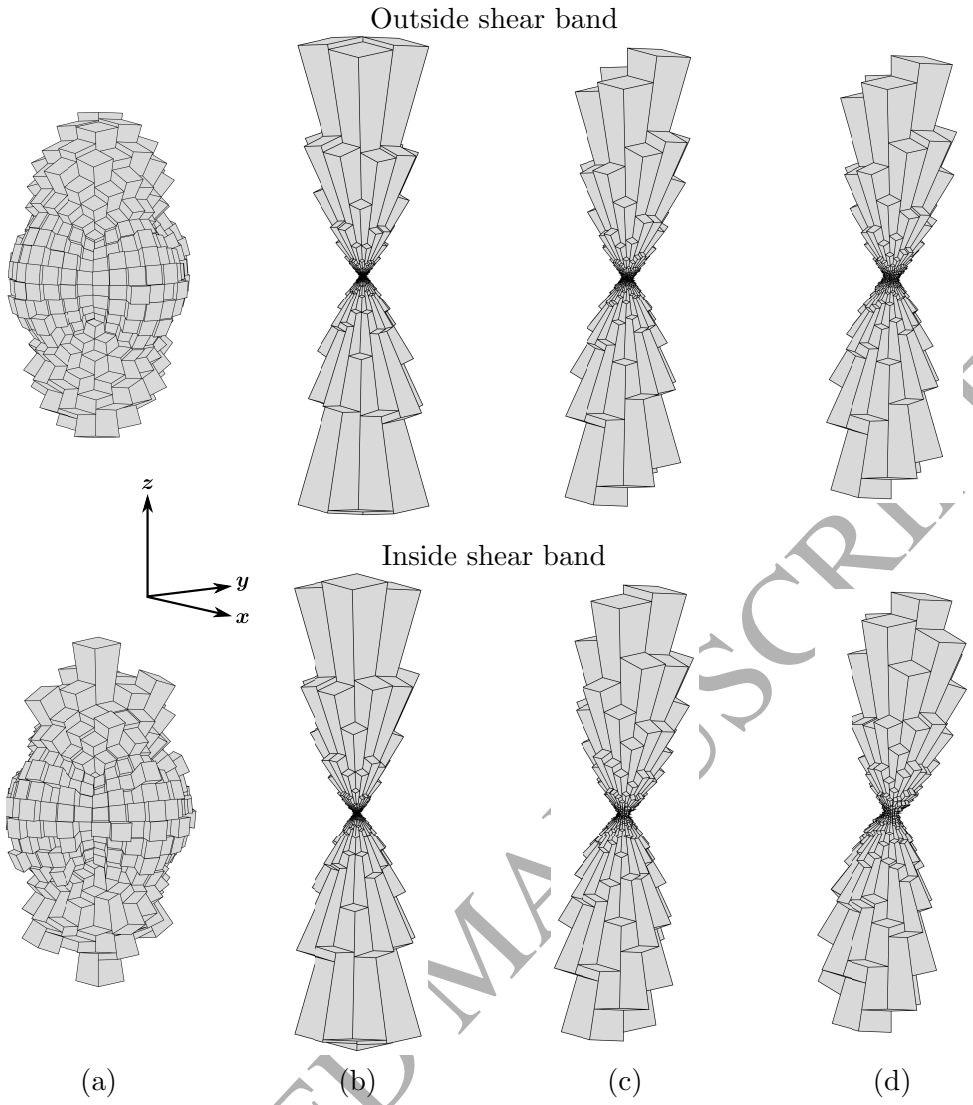

Figure 18: Spherical histograms of interparticle forces at (a) 0%, (b) 5%, (c) 10%, and (d) 15% axial strain, inside and outside the shear band. The distributions at 0% axial strain are computed using the shear band location at peak stress since the shear band does not yet exist at 0% axial strain.

Finally, the stress rotations occur in a plane defined by the same orientation angle ϕ shown in in Figure 15; that is, the orientation angle of the σ_1, once it deviates from the vertical (90°), is the same as the orientation angle of the shear band and the platen displacement. This further reinforces the notion of planar mechanics in the triaxial test despite it being 3-D.

7 Conclusions and Future Outlook

This study is the largest and most predictive undertaking of using a discrete model, LS-DEM, to quantitatively capture the results of a full triaxial test in real sands, and shows that LS-DEM not only can capture macroscopic behavior that is the classic stress-strain and volume-strain results of the triaxial test, but can also reproduce a shear band in a similar manner as the experiment, as well as local and particle scale quantities such as local deviatoric stress and particle rotations. Hence, the simulations show agreement with the experiments across macroscopic, local, and particle scales. Furthermore, the behavior of the shear band in the specimen is analyzed, leading to the following observations:

1. Shear strain localizes at an inclination that is the same as the inclination of the shear band that ultimately forms long before peak stress is achieved.

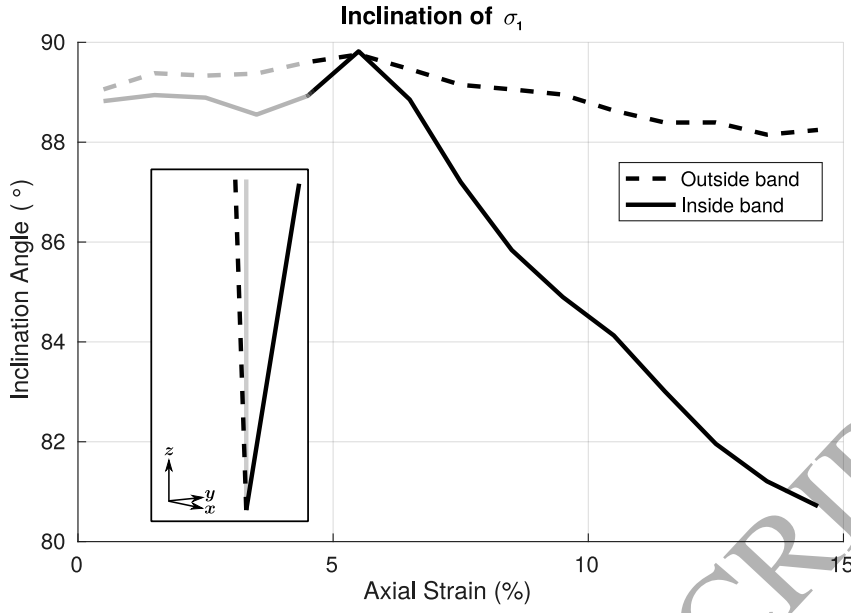

Figure 19: Inclination of the direction of the largest principal stress σ_1, both outside and inside the shear band. The grayed-out sections of the lines are computed using the shear band location at peak stress since the shear band does not exist prior to that. Inset: 3-D view of the direction of σ_1 outside and inside the shear band at the end of loading. The gray line is vertical (90°).

2. While the specimen appears to reach critical state, that is, at some point in loading, the volume and stress ratio become constant, the stress state continues to rotate.

3. The orientation angle of the shear band, platen displacement, and largest principal stress after it rotates away from the vertical all have the same value, suggesting that even through the triaxial test is three-dimensional, nearly all of the shear, deformation, and stress occur on a plane.

The results of this triaxial test, both experimental and computational, essentially represent a material point of Hostun sand that has been taken through a single loading path. Further experiments and simulations via the avatar paradigm are forthcoming; these would involve other stress paths like triaxial extension, cyclic loading, and true triaxial. Hopefully, the calibration of the LS-DEM model to one test would allow it to predict the results of the other tests. If this is true, it would make a very good case for the avatar paradigm to be a true "predictive" method allowing the probing of load paths that are impossible to perform experimentally, while starting from identical initial conditions. The sensitivity of strain localization to initial conditions can for the first time be probed quantitatively at the particle scale with such an avatar. Furthermore, XRCT is now able to adequately capture the surface roughness of the sand grains studied here, for a set of a few grains as the resolution needs to be much higher, which limits the window size. This opens the possibility of injecting higher-resolution LS-DEM particles into similar simulations to those presented to understand what scale of surface roughness is responsible for differences in the interparticle friction coefficient—experimentally, it makes a large difference [49]—and critically, the overall response.

To conclude, the avatar framework allows mechanical simulation of general particle shapes has been combined with a fine reproduction of an X-ray tomography triaxial experiment on complex, angular sand grains. The success of the reproduction of the grain and sample-scale mechanics indicate that the avatar paradigm may be able to simulate a great number of granular materials given their particle shapes. Furthermore, given the success in capturing the *constitutive* behaviour of the studied sample by injecting the shapes of its constituents means that we can cautiously state that we have an *in-silico* constitutive model for this material.

8 Acknowledgements

This work used the Extreme Science and Engineering Discovery Environment (XSEDE), which is supported by National Science Foundation grant number ACI-1548562 [55].

References

[1] K. A. Alshibli and S. Sture. Sand shear band thickness measurements by digital imaging techniques. *Journal of Computing in Civil Engineering*, 13(2):103–109, 1999.

[2] E. Andò, S. A. Hall, G. Viggiani, and J. Desrues. Experimental micro-mechanics of granular media studied by x-ray tomography: recent results and challenges. *Géotechnique Letters*, 3:142–146, 2013.

[3] E. And. *Experimental investigation of micro-structural changes in deforming granular media using x-ray tomography*. PhD thesis, Universit de Grenoble, 2013.

[4] E. And, S. A. Hall, G. Viggiani, J. Desrues, and P. Bsuelle. Grain-scale experimental investigation of localised deformation in sand: a discrete particle tracking approach. *Acta Geotechnica*, 7(1):1–13, 2012a.

[5] K. Bagi. Analysis of microstructural strain tensors for granular assemblies. *International Journal of Solids and Structures*, 43(10):3166 – 3184, 2006.

[6] D. Ballhause, M. König, and B. Kröplin. *Modelling Fabric-Reinforced Membranes with the Discrete Element Method*, pages 51–67. Springer Netherlands, Dordrecht, 2008.

[7] S. Beucher and C. Lantujoul. Use of watersheds in contour detection. In *Proc. of International workshop on image processing, real-time edge and motion detection*, September 1979.

[8] M. D. Bolton. The strength and dilatancy of sands. *Gotechnique*, 36(1):65–78, 1986.

[9] R. I. Borja and J. E. Andrade. Critical state plasticity. part vi: Meso-scale finite element simulation of strain localization in discrete granular materials. *Computer Methods in Applied Mechanics and Engineering*, 195(3740):5115 – 5140, 2006. John H. Argyris Memorial Issue. Part I.

[10] G. C. Cho, J. Dodds, and J. C. Santamarina. Particle shape effects on packing density, stiffness, and strength: Natural and crushed sands. *Journal of Geotechnical and Geoenvironmental Engineering*, 132(5):591–602, 2006.

[11] J. Christoffersen, M. M. Mehrabadi, and S. Nemat-Nasser. A micromechanical description of granular material behavior. *Journal of Applied Mechanics*, 48:339–344, 1981.

[12] M. B. Cil and K. A. Alshibli. 3d analysis of kinematic behavior of granular materials in triaxial testing using dem with flexible membrane boundary. *Acta Geotechnica*, 9(2):287–298, 2014.

[13] P. A. Cundall and O. D. L. Strack. A discrete numerical model for granular assemblies. *Géotechnique*, 29:47–65, 1979.

[14] B. Ebrahimian, A. Noorzad, and M. I. Alsaleh. Modeling shear localization along granular soil-structure interfaces using elasto-plastic cosserat continuum. *International Journal of Solids and Structures*, 49(2):257 – 278, 2012.

[15] W. Ehlers and B. Scholz. An inverse algorithm for the identification and the sensitivity analysis of the parameters governing micropolar elasto-plastic granular material. *Archive of Applied Mechanics*, 77(12):911, Sep 2007.

[16] P. Fu and Y. F. Dafalias. Fabric evolution within shear bands of granular materials and its relation to critical state theory. *International Journal for Numerical and Analytical Methods in Geomechanics*, 35(18):1918–1948, 2011.

[17] V. Galavi and H. F. Schweiger. Nonlocal multilaminate model for strain softening analysis. *International Journal of Geomechanics*, 10(1):30–44, 2010.

[18] H. Gao and O. Chae. Touching tooth segmentation from ct image sequences using coupled level set method. In *Visual Information Engineering, 2008. VIE 2008. 5th International Conference on*, pages 382–387, 2008.

[19] R. Gao, X. Du, Y. Zeng, Y. Li, and J. Yan. A new method to simulate irregular particles by discrete element method. *Journal of Rock Mechanics and Geotechnical Engineering*, 4(3):276 – 281, 2012.

[20] X. Garcia, J.-P. Latham, J. Xiang, and J. Harrison. A clustered overlapping sphere algorithm to represent real particles in discrete element modelling. *Geotechnique*, 59:779–784, 2009.

[21] P. Guo. Critical length of force chains and shear band thickness in dense granular materials. *Acta Geotechnica*, 7(1):41–55, 2012.

[22] R. Hart, P. A. Cundall, and J. Lemos. Formulation of a three-dimensional distinct element model - Part II: Mechanical calculations for motion and interaction of a system composed of many polyhedral blocks. *International Journal of Rock Mechanics and Mining Sciences*, 25(3):117–125, 1988.

[23] J. Hsieh. *Computed Tomography: Principles, Design, Artifacts, and Recent Advances*. SPIE Press monograph. SPIE Press, 2003.

[24] R. Hurley, S. Hall, J. Andrade, and J. Wright. Quantifying interparticle forces and heterogeneity in 3d granular materials. *Physical Review Letters*, 117(9):098005, 2016.

[25] M. Jean. The non-smooth contact dynamics method. *Computer Methods in Applied mechanics and Engineering*, 177(3-4):235–257, 1999.

[26] A. X. Jerves, R. Y. Kawamoto, and J. E. Andrade. Effects of grain morphology on critical state: a computational analysis. *Acta Geotechnica*, 11(3):493–503, 2016.

[27] K. Johnson and K. Johnson. *Contact Mechanics*. Cambridge University Press, 1987.

[28] C. Kafadar and A. Eringen. Micropolar mediai the classical theory. *International Journal of Engineering Science*, 9(3):271 – 305, 1971.

[29] K. Kanatani. Distribution of directional data and fabric tensors. *International Journal of Engineering Science*, 22(2):149–164, 1984.

[30] R. Kawamoto, E. Andò, G. Viggiani, and J. E. Andrade. Level set discrete element method for three-dimensional computations with triaxial case study. *Journal of the Mechanics and Physics of Solids*, 91:1 – 13, 2016.

[31] S. J. Lee, Y. M. Hashash, and E. G. Nezami. Simulation of triaxial compression tests with polyhedral discrete elements. *Computers and Geotechnics*, 43:92 – 100, 2012.

[32] C. Li, C. Xu, C. Gui, and M. Fox. Distance regularized level set evolution and its application to image segmentation. *Image Processing, IEEE Transactions on*, 19(12):3243–3254, Dec 2010.

[33] T. Li, Y. Peng, Z. Zhu, S. Zou, and Z. Yin. Discrete element method simulations of the inter-particle contact parameters for the mono-sized iron ore particles. *Materials*, 10, 2017.

[34] K. Lim, R. Kawamoto, E. Andò, G. Viggiani, and J. Andrade. Multiscale characterization and modeling of granular materials through a computational mechanics avatar: a case study with experiment. *Acta Geotechnica*, 2015.

[35] K.-W. Lim and J. E. Andrade. Granular element method for three-dimensional discrete element calculations. *International Journal for Numerical and Analytical Methods in Geomechanics*, 38(2):167–188, 2014.

[36] G. MiDi. On dense granular flows. *The European Physical Journal E*, 14(4):341–365, 2004.

[37] D. Muir Wood. *Soil behaviour and critical state soil mechanics*. Cambridge University Press, Cambridge, England, 1990.

[38] H. B. Mhlhaus and I. Vardoulakis. The thickness of shear bands in granular materials. *Gotechnique*, 37(3):271–283, 1987.

[39] P. L. Newland and B. H. Allely. Volume changes in drained taixial tests on granular materials. *Gotechnique*, 7(1):17–34, 1957.

[40] M. Oda. Initial fabrics and their relations to mechanical properties of granular materials. *Soils and Foundations*, 12:17–36, 1972.

[41] N. Otsu. A threshold selection method from gray-level histograms. *IEEE Transactions on Systems, Man, and Cybernetics*, 9(1):62–66, Jan 1979.

[42] A. L. Rechenmacher and R. J. Finno. Digital image correlation to evaluate shear banding in dilative sands. *Geotechnical Testing Jounal, ASCE*, 27:1–10, 2004.

[43] J. Rice. The localization of plastic deformation. In *in: W.T. Koiter (Ed.), Theoretical and Applied Mechanics*, pages 207–220. North-Holland Publishing Company, 1976.

[44] K. H. Roscoe. The influence of strains in soil mechanics. *Gotechnique*, 20(2):129–170, 1970.

[45] L. Rothenburg and R. J. Bathurst. Analytical study of induced anisotropy in idealized granular materials. *Géotechnique*, 39:601–614, 1989.

[46] L. Rothenburg and R. J. Bathurst. Numerical simulation of idealized granular assemblies with plane elliptical particles. *Computers and Geotechnics*, 11(4):315 – 329, 1991.

[47] P. W. Rowe. The stress-dilatancy relation for static equilibrium of an assembly of particles in contact. *Proceedings of the Royal Society of London A: Mathematical, Physical and Engineering Sciences*, 269(1339):500–527, 1962.

[48] J. Rudnicki and J. Rice. Conditions for the localization of deformation in pressure-sensitive dilatant materials. *Journal of the Mechanics and Physics of Solids*, 23(6):371 – 394, 1975.

[49] C. Sandeep and K. Senetakis. Exploring the micromechanical sliding behavior of typical quartz grains and completely decomposed volcanic granules subjected to repeating shearing. *Energies*, 10:370, 2017.

[50] A. Schofield and P. Wroth. *Critical State Soil Mechanics*. McGraw-Hill, New York, 1968.

[51] J. Sulem and I. Vardoulakis. *Bifurcation analysis in geomechanics*. CRC Press, 2004.

[52] Y. Sun and Y. Xiao. Fractional order plasticity model for granular soils subjected to monotonic triaxial compression. *International Journal of Solids and Structures*, 118(Supplement C):224 – 234, 2017.

[53] J. Tejchman. *Shear Localization in Granular Bodies with Micro-Polar Hypoplasticity*. Springer-Verlag Berlin Heidelberg, 2008.

[54] J. M. Ting, M. Khwaja, L. R. Meachum, and J. D. Rowell. An ellipse-based discrete element model for granular materials. *International Journal for Numerical and Analytical Methods in Geomechanics*, 17(9):603–623, 1993.

[55] J. Towns, T. Cockerill, M. Dahan, I. Foster, K. Gaither, A. Grimshaw, V. Hazlewood, S. Lathrop, D. Lifka, G. D. Peterson, R. Roskies, J. R. Scott, and N. Wilkins-Diehr. Xsede: Accelerating scientific discovery. *Computing in Science & Engineering*, 16(5):62–74, 2014.

[56] I. Vlahinic, E. Ando, G. Viggiani, and J. E. Andrade. Towards a more accurate characterization of granular media: extracting quantitative descriptors from tomographic images. *Granular Matter*, pages 1–13, 2013. doi:10.1007/s10035-013-0460-6.

[57] I. Vlahinić, R. Kawamoto, E. Andò, G. Viggiani, and J. E. Andrade. From computed tomography to mechanics of granular materials via level set bridge. *Acta Geotechnica*, 12(1):85–95, 2017.

[58] O. R. Walton and R. L. Braun, editors. *Simulation of rotary-drum and repose tests for frictional spheres and rigid sphere clusters*, Nov. 1993.

[59] B. Yan, R. A. Regueiro, and S. Sture. Threedimensional ellipsoidal discrete element modeling of granular materials and its coupling with finite element facets. *Engineering Computations*, 27(4):519–550, 2010.

[60] J. Zheng and R. D. Hryciw. An image based clump library for dem simulations. *Granular Matter*, 19(2):26, Mar 2017.